EFFECTS OF ARBITRARY SHAPED SURFACE TOPOGRAPHIES ON EARTHQUAKE GROUND MOTION USING BOUNDARY ELEMENT METHOD IN TIME DOMAIN[*]

M. RAHIMIAN[1**], B. OMIDVAR[2], H. DERAKHSHAN[1] AND A. NOORZAD[1]

[1]Dept. of Civil Engineering, University of Tehran, Tehran, I. R. of Iran
Email: rahimian@ut.ac.ir
[2]Faculty of Environmental Engineering, University of Tehran, Tehran, I. R. of Iran

Abstract– In this paper, the direct boundary element method in time domain is used for the calculation of local amplifications of seismic waves by real 3-dimensional surface topographies. The presented method is effective for modelling surface irregularities with arbitrary shapes under complex incident wave forms. A real topography with particular importance in Iran, Urmia Hill, which represents a complex surface irregularity with sloping boundaries, is considered as a study case and its seismic behaviour, particularly sloping boundary effects, is studied under *SH* and *SV* incident waves with various azimuths and angles of incidence. This method can equally be used for P or mixed P-S incidences. The boundary is modelled using quadrilateral (8-node) elements, and synthetic displacement time history based on the deterministic approach is used for excitation of the model. The results show that the areas located at the end of slopes experience more excitations in some cases, while greater amplifications occur in the nearby flat areas in some other incidences. The amplification pattern is shown to be completely dependent on the wave type and the direction of sloped boundaries with respect to the angle and azimuth of incidence.

Keywords– Wave propagation, time domain boundary element method, topography effects, amplification, Urmia

1. INTRODUCTION

In recent earthquakes, certain damage patterns have been observed on earthquake-stricken sites [1, 2]. This phenomenon has encouraged researchers to look for the reasons and many researches have been done. The works, however, are very different, either on approach or field of study. Although many simplified irregularities have been taken under consideration for a wave propagation study in the frequency domain, far fewer researches have been done to observe the problem in the time domain. Sanchez-sesma [3] and Eshraghi and Dravinsky [4] suggested simple models for the investigation of wave motion. Non-symmetrical models have also been established by many researchers; Semblat *et al.* [5] used BEM for studying the response of the area of Nice (France) under synthetic seismographs. Reinoso [6] considered the time response of topographies by Fourier Transform of the spectral displacements. Kamalian *et al*. [7] used a time domain two-dimensional BEM to investigate the effects of regular geometries on incident body and surface waves.

In many of these works, the boundary element method has continuously proved to be more effective for introducing half space characteristics in the process. This is due to the fact that it satisfies the radiation condition and leads to a reduced system of equations during the solution process.

2. STATEMENT OF THE PROBLEM

Figure 1 illustrates a domain Ω with an arbitrary boundary Γ excited by an incident wave $f[t]$, in which $[\ ]$ stands for a discrete time history. In this situation, in addition to the free field displacements produced by the incident wave, a late field of waves known as "Scattered Field" will also be produced in edges and corners of the site. Therefore, the total field of displacements will be in two parts:

$$u^t = u^s + u^i \tag{1}$$

u^t, u^s and u^i in Eq. (1) are total, scattered and free field displacement vectors, respectively. Considering flat wave propagation, Eq. (2) can be written for the excitation of any point of the site:

$$f[\tau] = f[t - \frac{d}{c}] \tag{2}$$

Where, d is the distance from the wave front, τ indicates the local time reference for each node, t is total reference time computed from the beginning of the calculations, and c is the velocity of the incident wave. Using Mathematics and assuming a planar wave front, the distance d can be expressed by Eq. (3):

$$d = a_1(x - x_1) + a_2(y - y_1) + a_3(z - z_1) + nc\Delta t \tag{3}$$

Where a_1 to a_3 are components of wave normal and $n\Delta t$ is introduced for easier handling of time incidence and is defined as the first time a wave arrives to point A, the closest point of the site. Substituting d from Eq. (3) in Eq. (2), we have:

$$f[\tau] = f[t - n\Delta t - \frac{a_1(x - x_1) + a_2(y - y_1) + a_3(z - z_1)}{c}] \tag{4}$$

Equation (4) represents the incident wave as a function of spatial coordinates. Therefore the spatial derivative of the wave function can easily be found and then the free field traction vectors in each point of the domain.
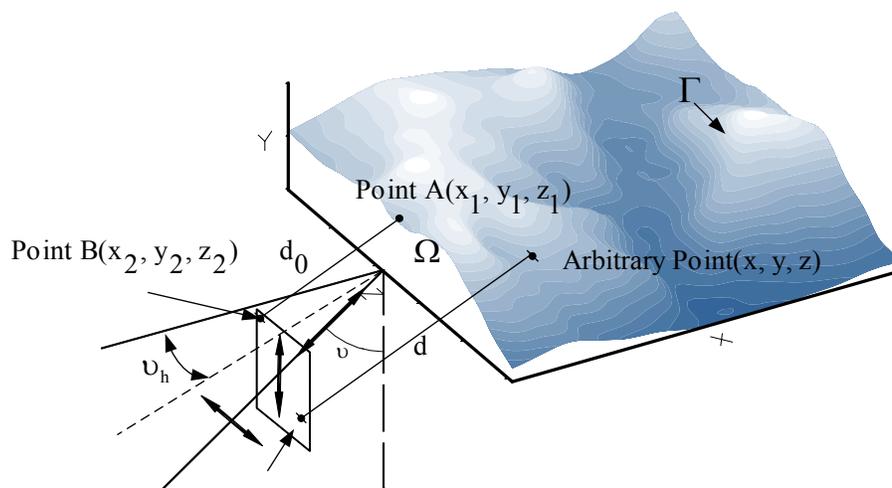
Fig. 1. Wave front position with respect to an arbitrary shaped topography

a) Free and scattered fields of displacements

Once Eq. (4) is established, free field displacement and traction vectors, i.e. $\boldsymbol{u}^i$ and $\boldsymbol{t}^i$, will be found using the elasticity theory and the following expressions:

$$u_i^i = a_i f[\tau],$$ (5)

$$\frac{\partial u_i^i}{\partial x_j} = a_i \frac{\partial f[\tau]}{\partial x_j},$$ (6)

$$\frac{\partial f[\tau]}{\partial x_i} = -\frac{a_i}{c} \frac{\partial f[\tau]}{\partial t},$$ (7)

in order to compute the complete field of displacements, the free traction boundary condition should be satisfied over the topography surface. For this purpose, a compensation traction vector $\boldsymbol{t}^s$, which is equal but opposite to $\boldsymbol{t}^i$, should be applied on the boundary as a boundary condition for the Navier equation, and then we have:

$$\mu u_{i,jj}^s + (\lambda + \mu) u_{j,ij}^s - \rho \frac{\partial^2 u_i^s}{\partial t^2} = 0,$$

$$t_i^s = -t_i^i \ on \ \Gamma$$ (8)

Equation (8) will give us the scattered field of displacements $\boldsymbol{u}^s$. This vector will be added to $\boldsymbol{u}^i$ using Eq. (1) to compose the total displacement field.

3. BOUNDARY ELEMENT FORMULATION

We use BEM to solve Eq. (8). Writing a reciprocity theorem between the real problem situation and the infinite solution leads to the following governing integral equation:

$$u_i(\boldsymbol{X}',t) =$$
$$\int_0^t \left[\int_\Gamma U_{ij}(\boldsymbol{X}',t,\boldsymbol{x},\tau) t_j(\boldsymbol{x},\tau) d\Gamma(\boldsymbol{x}) \right] d\tau$$
$$- \int_o^t \left[\int_\Gamma T_{ij}(\boldsymbol{X}',t,\boldsymbol{x},\tau) u_j(\boldsymbol{x},\tau) d\Gamma(\boldsymbol{x}) \right] d\tau$$ (9)

Where $u_j(\boldsymbol{x},\tau)$ and $t_j(\boldsymbol{x},\tau)$ are displacement and traction at time τ in point $\boldsymbol{x}$. $\boldsymbol{X}'$ is an interior point. $U_{ij}(\boldsymbol{X}',t,\boldsymbol{x},\tau)$ and $T_{ij}(\boldsymbol{X}',t,\boldsymbol{x},\tau)$ are fundamental solutions for the time domain and can be found in [8]. Transferring point $\boldsymbol{X}'$ to the boundary, Eq. (9) can be written as:

$$c_{ij} u_j(\boldsymbol{x}',t) =$$
$$\int_0^t \int_\Gamma U_{ij}(\boldsymbol{x}',t,\boldsymbol{x},\tau) t_j(\boldsymbol{x},\tau) d\Gamma(\boldsymbol{x}) d\tau$$
$$- \int_o^t \int_\Gamma T_{ij}(\boldsymbol{x}',t,\boldsymbol{x},\tau) u_j(\boldsymbol{x},\tau) d\Gamma(\boldsymbol{x}) d\tau$$ (10)

Where $c_{ij} = \delta_{ij}/2$, if the boundary is smooth. If the boundary is not smooth it should be computed using a different procedure [6]. Equaion (10) represents BIE for the problem, which can be solved over the discretized boundary by the collocation method. When the collocation point is a node of the computing

element, singular integrals will be produced. These integrals are evaluated using an algorithm proposed by Guiggiani and Gigante [9], in which singular kernel subtraction is implemented using a Taylor expansion in the neighbourhood of the singular point [10]. Omidvar [11] produced a general-purpose Boundary Element Method Code for time and frequency domain analysis of Elastodynmic problems. We use this code in our analyses.

4. NUMERICAL ASPECTS

Enough number of elements should be chosen for a reasonable representation of surface irregularities. The length of elements (L), however, is limited to a value according to wave velocity and time step. Many analyses have been done to test the numerical convergence of the method. Eq. (11) has been suggested for computing the length of time steps:

$$c\Delta t = 0.85L, \qquad i = 1,2 \tag{11}$$

In the above equation, L, the length of the element, is defined as the longest distance between the surrounded nodes of the element. Manolis and Beskos [12] suggested that this ratio be between 0.55 and 1.

   If we want to use this method for a mixed P-S wave propagation stage we should determine the time steps according to some additional factors including different wave velocities.

5. VALIDATION OF THE METHOD

A hemispherical canyon of one meter in depth has been considered under a vertical SH-wave incidence by Reinoso [6]. Mechanical properties of the ambient have been assumed to be 1 for shear and longitudinal wave velocities, and 0.333 for Poisson ratio. The problem then is solved in the frequency domain for a series of different frequencies. For an individual dimensionless frequency of 0.75, the results are given in Fig. 2, and are then compared with our results.
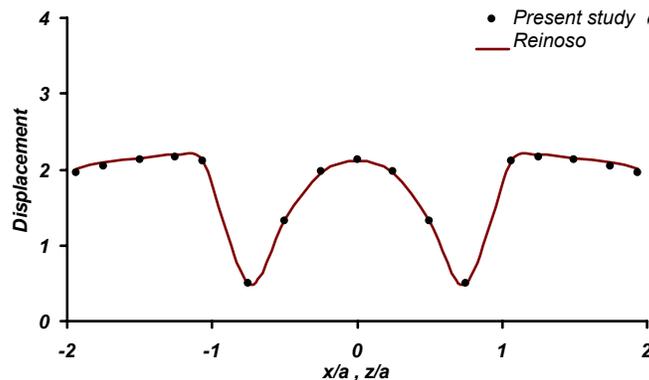
Fig. 2. Displacement at point x or z from center of canyon (a: radius)

6. URMIA TOPOGRAPHY

Urmia topography, with an area of 6 * 7 km^2, is a part of Urmia, a city with a population of almost 1 million, located in the N-W of Iran. Two long 20% slopes cross parts of this topography. These slopes, accompanied by flat and dome shaped ends, compose a complex surface topography. We have considered several incidences and studied the amplification pattern that has occurred in each case. Figs. 3, 4 and 5 show the site, its middle sections and contour map. Geological founding and field tests give the main soil layer properties as below:

$\rho = 1800 kg / m^3, \alpha = 585 m / s, \beta = 358 m / s$ giving *Poisson ratio=0.2, E=554 MPa*
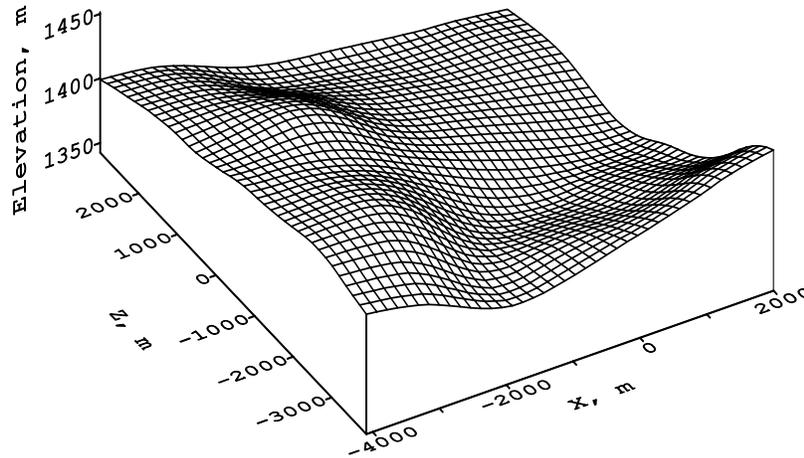
Fig. 3. Urmia topography
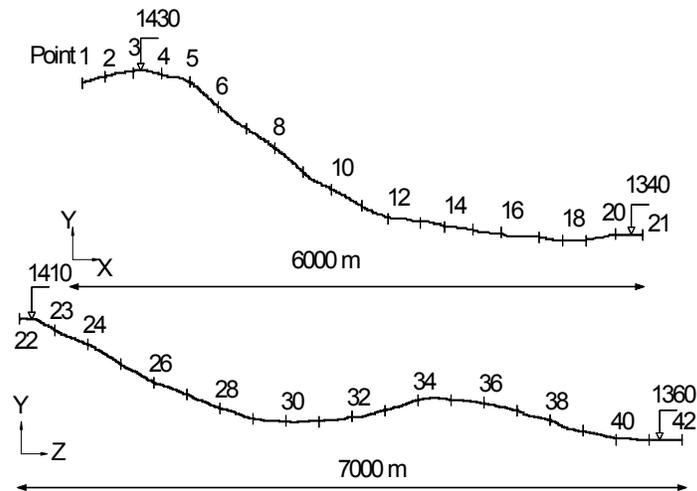
Fig. 4. Two middle sections of the site, selected points

A deterministic approach has been used for preparing site displacement spectra (Fig. 6a), and an iterative modification process in the frequency domain considering site seismic characteristics is utilized to convert relevant earthquake time history to artificial seismic displacement time history (Fig. 6b), having the target displacement spectra [13]. The boundary has been discretized into 100 (8-node) boundary elements with 341 nodes. Incident waves are assumed to propagate from the negative side of the Cartesian coordination system toward the site. Figure 7 to 19 include the results of the analyses in the form of amplification factors computed for *SH* and *SV* incidences. The problem is solved for two different azimuths of 0 and 90, and in each case for vertical incidence and oblique 30 and 60 incidences. The amplification factor is calculated based on the incident wave amplitude. Hence, for a flat surface under vertical incidences, the amplification factor is 2.

Fig. 5. Contour map

(a)   (b)
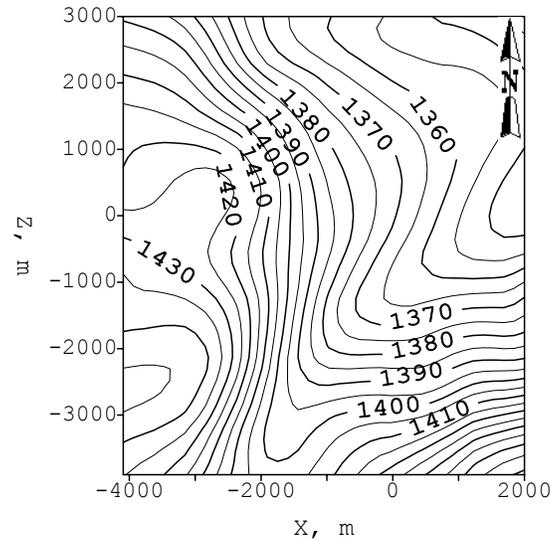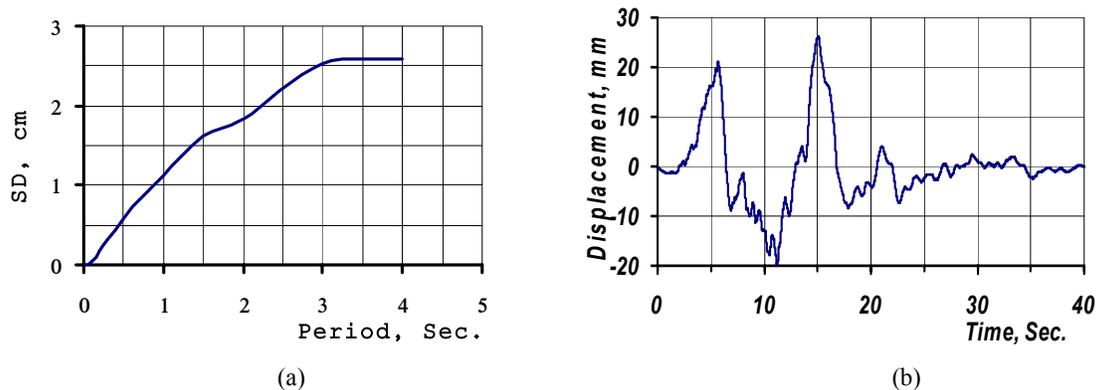
Fig. 6. a) Site displacement spectra, b) Synthetic displacement time history

Figure 7 shows the dependence of amplifications on the angle of incidence along the first section (Fig. 4), for an azimuth of zero. For an increase in the angle of incidence from 0 to 30, there is a rise in amplifications, particularly in sites 6 to 8. Amplification peaks on site 7 by a value of 7.5, a 60-incidence however produces less amplification. The fact that this angle is far larger than the critical angle for transversal incidences may have affected the amplification pattern. Figure 8 is similar to 6, but for *u* component in *SV* waves. A reverse action of scattered waves can be observed just before and after the slope which is more visible in 60-incidence. Wave amplitudes in sites at the ends of the slope are more intensified. Figure 9 shows the dependence of amplifications on υ for the vertical component of *SV* waves. It can be seen that larger amplifications again occur on 30-incidence. In this figure more amplification is seen in points 6-12, which are located on the slope surface. Figures 10 and 11 show the dependence of amplifications on υ along the second section (Fig. 4) for *SV* incidence with an azimuth angle of 90. The reverse action of the scattering waves again can be seen, but this time along the *Z* direction. Although more amplification is seen for 60-incidence along the second section (Fig. 10), in 3-D plots it is found that the maximum overall amplifications still occur for 30-incidence. In Fig. 11, it is shown that the amplification pattern is slightly different for 30 and 60-incidences. More amplification occurs in sites 27 to 33 for 30-incidence, while sites 34-40 are more amplified in 60-incidence.
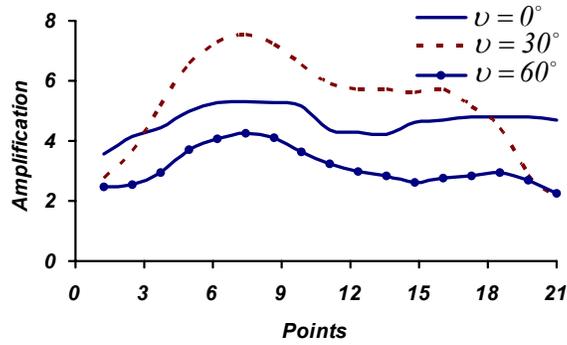
Fig. 7. Dependence of amplifications on υ, w component, *SH*, $\upsilon_h = 0$
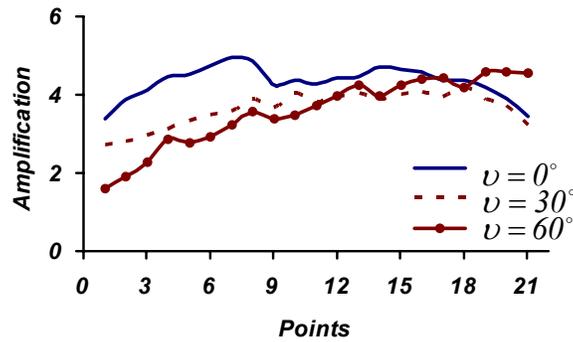
Fig. 8. Dependence of amplifications on υ, u component, *SV*, $\upsilon_h = 0$
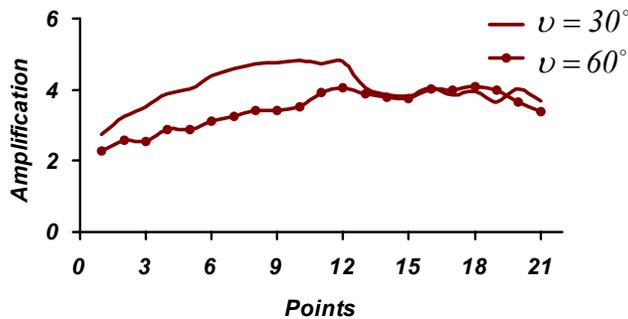
Fig. 9. Dependence of amplifications on υ, v component, *SV*, $\upsilon_h = 0$
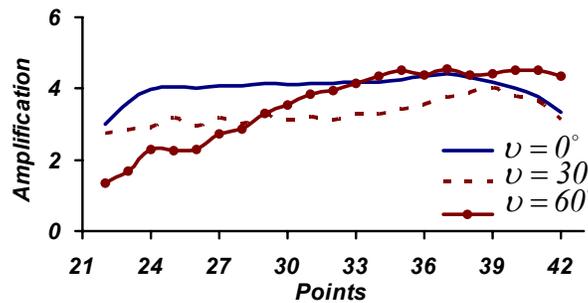
Fig. 10. Dependence of amplifications on υ, w component, *SV*, $\upsilon_h = 90$
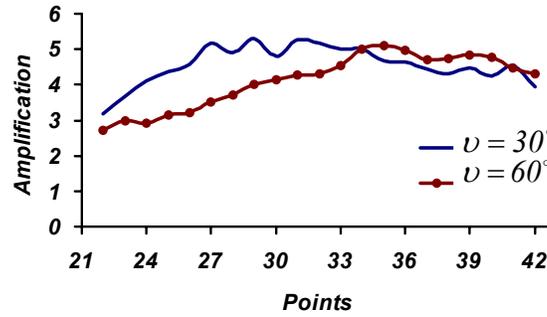
Fig. 11. Dependence of amplifications on υ, *v* component, *SV*, $\upsilon_h = 90$

Figures 12 to 19 illustrate the amplification pattern that has occurred during *SH* and *SV*-wave propagation with azimuth angles of $\upsilon_h = 0$ and $\upsilon_h = 90$, as a function of geometrical coordinates of the site and for several incident angles υ. Figures 12 and 13 show results for oblique *SH* incidences. It can be seen that regions located on the top of the irregularities experience more amplification than the other sites. These areas were greatly amplified (up to 400%) for 60-incidence and this is more intensified in 30-incidence (up to 730%). Figure 14 indicates that sites near the bottom end of the main slope are less amplified for vertical *SV* incidence. Figures 15 and 16 show the results for *SV* incidence with $\upsilon = 60$. It is seen that the vertical component of the oblique *SV* wave is more amplified than the horizontal component.
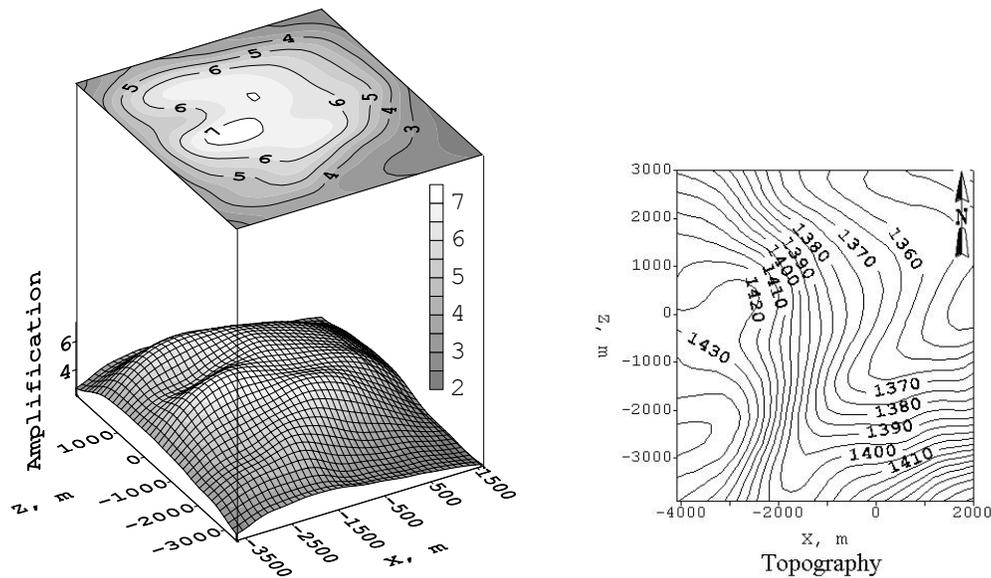
Fig. 12. Amplification for *w, SH* wave, $\upsilon_h = 0°$ and $\upsilon = 30$

Figure 17 shows the amplifications for the vertical component of an oblique *SV* wave with $\upsilon = 30$. In this figure it is shown that greater amplifications have occurred at the regions located on the cross section of the minor domes.

Figures 18 and 19 illustrate the amplifications of the horizontal and the vertical components of the *SV* 60-incidence. It can be seen that the overall amplification for the vertical component is greater than that of the horizontal component. Also, it can be observed that the reverse action of the scattered waves has reduced some of the effects of minor domes.
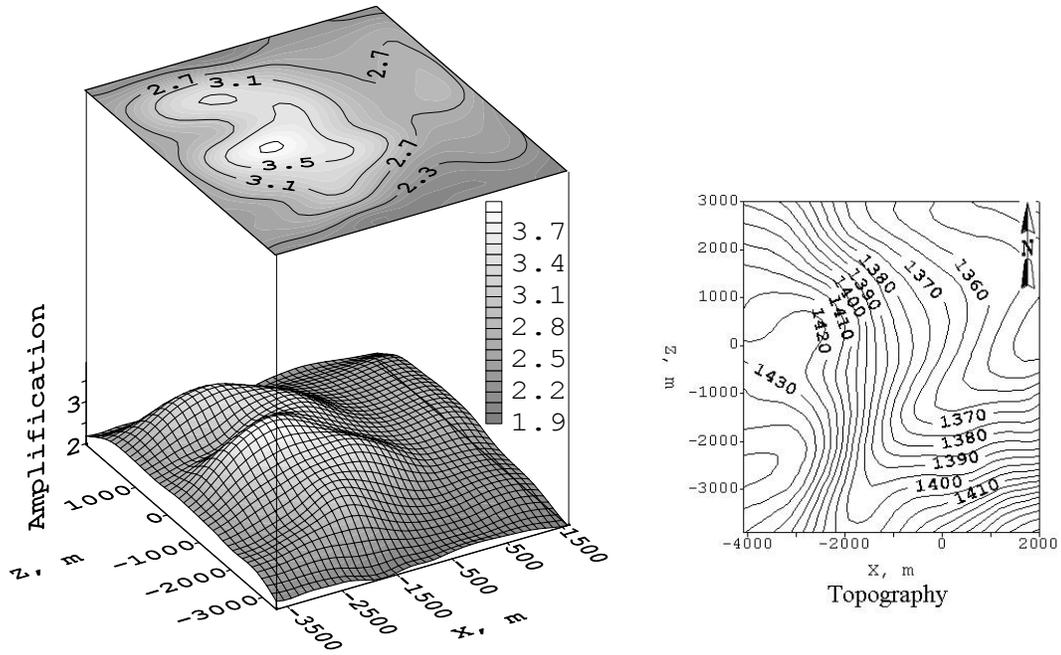
Fig. 13. Amplification for *w, SH* wave, $\upsilon_h = 0°$ and $\upsilon = 60$
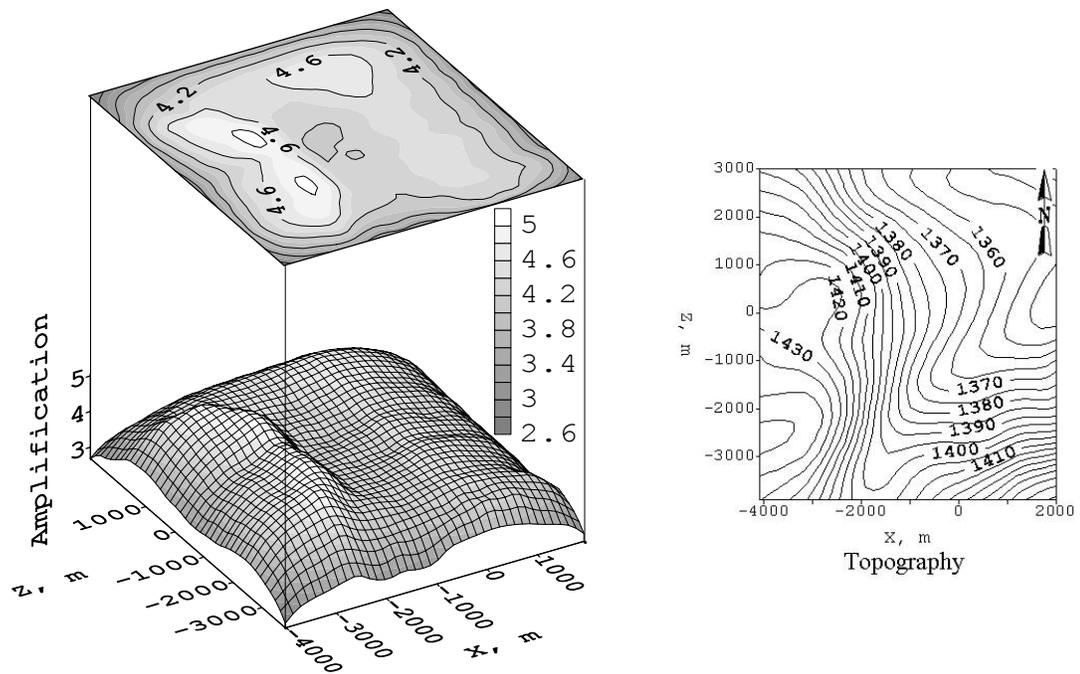
Fig. 14. Amplification for *u, SV* wave, $\upsilon_h = 0°$ and $\upsilon = 0$
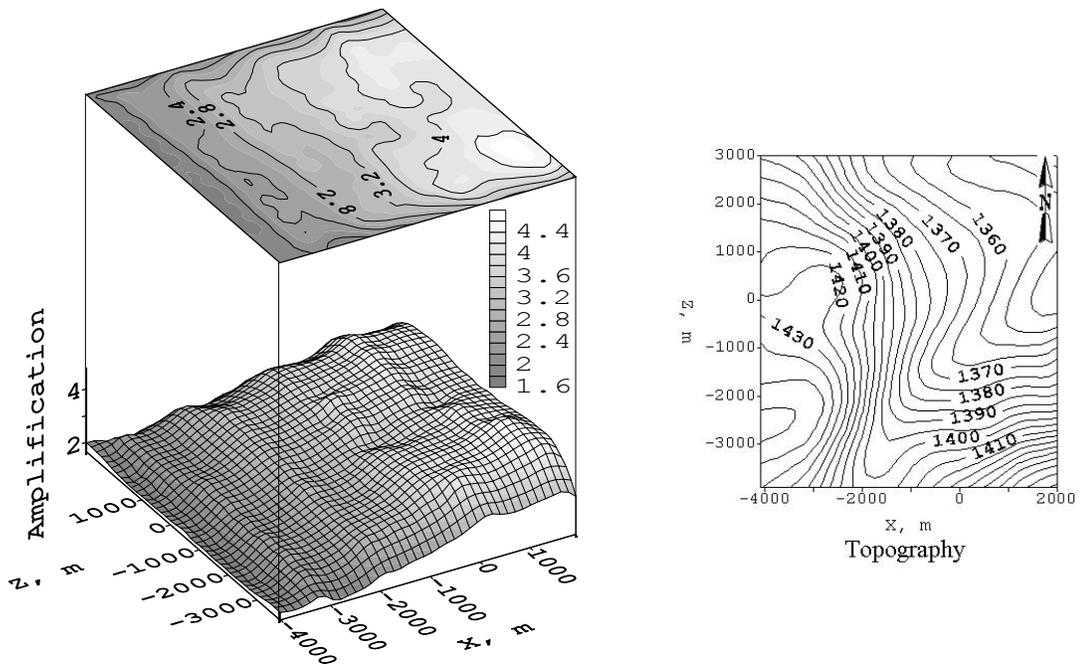
Fig. 15. Amplification for *u, SV* wave, $\upsilon_h = 0°$ and $\upsilon = 60$
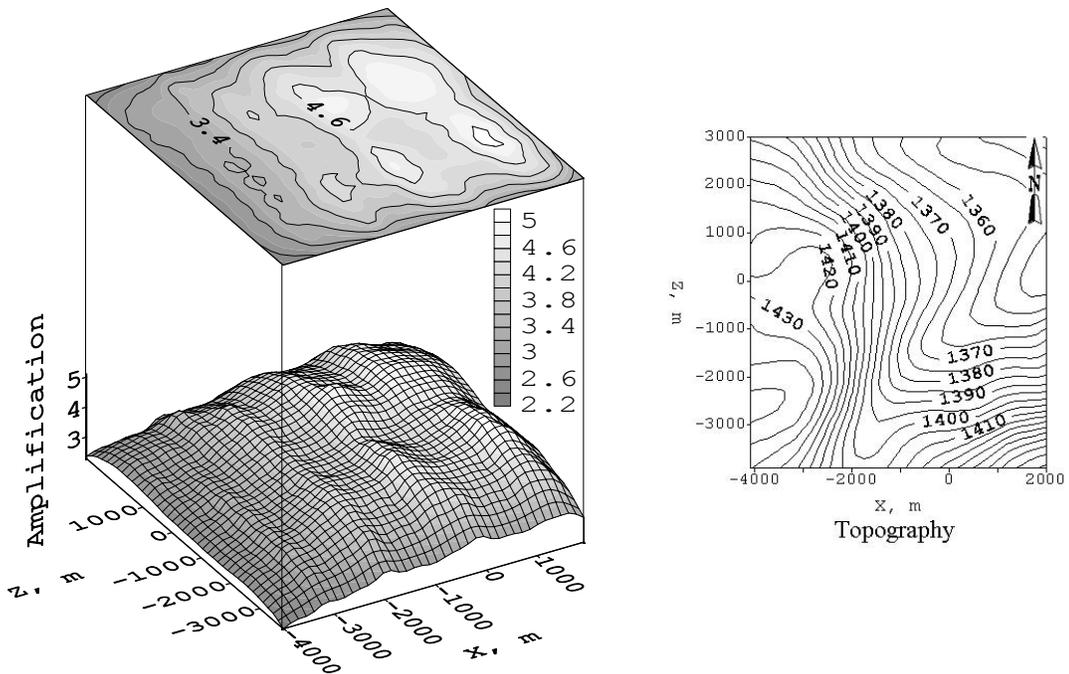
Fig. 16. Amplification for *v, SV* wave, $\upsilon_h = 0°$ and $\upsilon = 60$
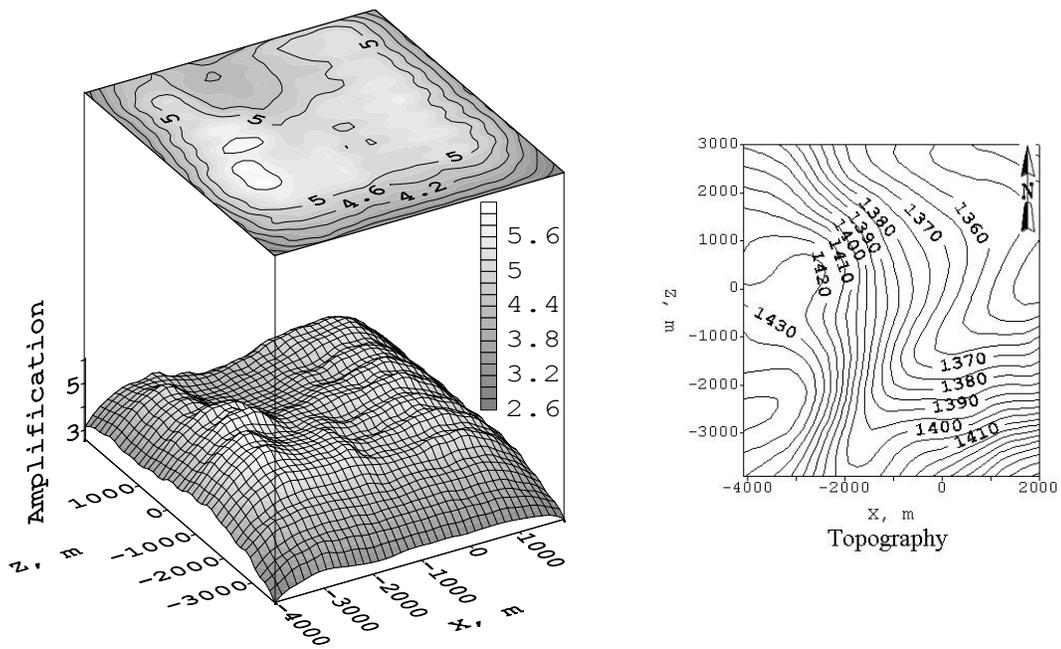
Fig. 17. Amplification for *v, SV* wave, $\upsilon_h = 90°$ and $\upsilon = 30$
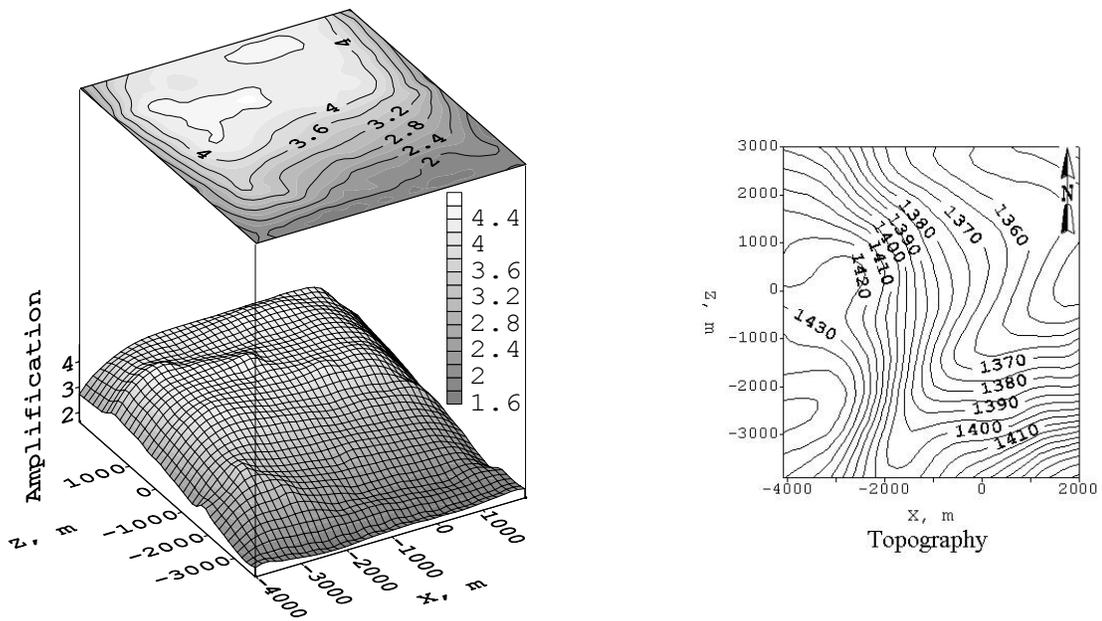
Fig. 18. Amplification for *w, SV* wave, $\upsilon_h = 90°$ and $\upsilon = 60$
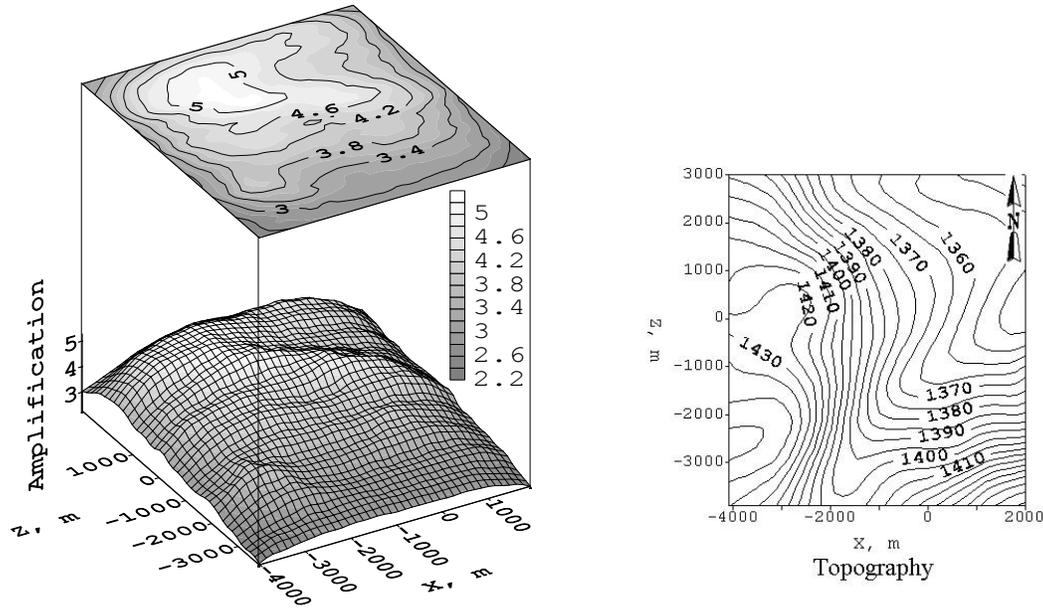
Fig. 19. Amplification for *v, SV* wave, $\upsilon_h = 90°$ and $\upsilon = 60$

7. CONCLUSIONS

An effective and simple method was introduced for the computation of the effects of arbitrary shaped topographies on the earthquake ground motions in a time domain. The effects of Urmia surface topography on earthquake ground motion was studied by establishing 3-D plots of the amplification pattern for several incidences. The response of the ground surface was analyzed by a time domain boundary element method code. Results show that in oblique $30°$-SV and SH-waves, the vertical component of motion is greatly amplified (750%) at the regions located near the end of the slope, whereas less amplification occurs at sites located on the slope. A reverse action of the scattering phenomenon in oblique incidences was detected. This behaviour seems to be in agreement with the theoretical findings. This phenomenon can dominate some of the effects of slopes and irregularities. It is also found that a combined system of domes and topographies produces a complicated amplification pattern and leads to greater excitations. Further, it is shown that, in contrast to common engineering beliefs, the amplification can be on the down hill not on the top of the hills. Finally it is concluded that the azimuth, angle of incidence, wave type and topography shape have important contributions in modifying the intensity of incident waves.

REFERENCES

1. Finn, W. D. L., Ventura, C. E. & Schuster, N. D. (1995). Ground motions during the 1994 Northridge earthquake. *Canadian Journal of Civil Engineering*, Vol. 22, No. 2, pp. 300-315.
2. Hiroshi, K. (1996). The cause of the damage belt in Kobe: "the basin-edge effect", constructive interference of the direct s-wave with the basin-induced diffracted Raleigh waves. *Seism. Res. Lett.*, Vol. 67, No. 5, pp. 25-30.
3. Sanchez-sesma, F. J. (1985). Diffraction of elastic SH waves by wedges. *Bull. Seism. Soc. Am.,* Vol. 75, pp. 1435-1446.
4. Eshraghi, H. & Dravinsky, M. (1989). Scattering of plane harmonic SH, SV, P and Rayl. Waves by non-axisymmetric 3-dim canyons: A wave function expansion approach, *Int. J. Earth. Eng. Str. Dyn.,* Vol. 18, pp. 983-998.

5. Semblat, J. F., Duval, A. M. & Dangla, P. (2000). Numerical analysis of seismic wave amplification in Nice (France) and comparison with experiments, *J. of Soil Dyn. and Earth. Eng.,* Vol. 19, pp. 347-362.

6. Reinoso, E. (2002). *Scattering of Seismic Waves: Applications to Mexico City Valley*, WIT press: London.

7. Kamalian, M., Gatmiri, B. & Sohrabi, B. A. (2003). On time-domain two-dimensional site response analysis of topographic structures by BEM, *JSEE*, Vol. 5, No 2.

8. Wen, P. H., Aliabadi, M. H. & Young, A. (1999). A time-dependent formulation of dual bem for 3D dynamic crack problems, *Int. J. Num. Methods Eng.*, Vol. 45, pp. 1887-1905.

9. Guiggiani, M. & Gigante, A. (1990). A general algorithm for multidimensional Cauchy principal value integrals in the boundary element method, *J. of App. Mech.*, Vol. 57, pp. 906-914.

10. Aliabadi, M. H., Hall, W. S. & Phemister, T. G. (1985). Taylor expansions for singular kernels in the boundary element method, *Int.J. Num. Methods Engng*, Vol. 21, pp. 2221-2236.

11. Omidvar, B. (2003). *PhD Thesis,* University of Tehran, Tehran, Iran.

12. Manolis, G. D. & Beskos, D. E. (1988). *Boundary Element Methods in Elastodynamics*, Hyman: London.

13. Rahimian, M., Omidvar, B., Noorzad, A. & Derakhshan, H. (2003). *Effects of topographies on earthquake ground motion in a few mountain- neighbored cities.* Second report to National Disaster Task Force, Earthquake and Land Slide Hazards Committee, Tehran, Iran.